Tectonophysics 677–678 (2016) 34–44

Contents lists available at ScienceDirect

Tectonophysics

journal homepage: www.elsevier.com/locate/tecto

Seismicity and fault geometry of the San Andreas fault around Parkfield, California and their implications

Woohan Kim [a], Tae-Kyung Hong [b,*], Junhyung Lee [b], Taka'aki Taira [c]

[a] Gyeongsang National University, Department of Earth and Environmental Sciences and RINS, Jinju, Gyeongsangnam-do 660-701, South Korea
[b] Yonsei University, Department of Earth System Sciences, 50 Yonsei-ro, Seodaemun-gu, Seoul 120-749, South Korea
[c] Berkeley Seismological Laboratory, University of California, Berkeley, CA 94720, USA

ARTICLE INFO

Article history:
Received 10 July 2015
Received in revised form 30 January 2016
Accepted 23 March 2016
Available online 07 April 2016

Keywords:
Fault geometry
Velocity anomalies
Local seismicity
San Andreas fault
Parkfield

ABSTRACT

Fault geometry is a consequence of tectonic evolution, and it provides important information on potential seismic hazards. We investigated fault geometry and its properties in Parkfield, California on the basis of local seismicity and seismic velocity residuals refined by an adaptive-velocity hypocentral-parameter inversion method. The station correction terms from the hypocentral-parameter inversion present characteristic seismic velocity changes around the fault, suggesting low seismic velocities in the region east of the fault and high seismic velocities in the region to the west. Large seismic velocity anomalies are observed at shallow depths along the whole fault zone. At depths of 3–8 km, seismic velocity anomalies are small in the central fault zone, but are large in the northern and southern fault zones. At depths >8 km, low seismic velocities are observed in the northern fault zone. High seismicity is observed in the Southwest Fracture Zone, which has developed beside the creeping segment of the San Andreas fault. The vertical distribution of seismicity suggests that the fault has spiral geometry, dipping NE in the northern region, nearly vertical in the central region, and SW in the southern region. The rapid twisting of the fault plane occurs in a short distance of approximately 50 km. The seismic velocity anomalies and fault geometry suggest location-dependent piecewise faulting, which may cause the periodic M6 events in the Parkfield region.

1. Introduction

Fault structure and geometry are useful indicators of fault mechanics and seismic behavior. Seismic reflection and refraction studies have been found to be useful for investigation of fault properties (Louie et al., 1988; Fuis et al., 2001; Catchings et al., 2002; Lutter et al., 2004; Hole et al., 2006; Zhao et al., 2010). Low-velocity fault zones have been well mapped in seismic tomography studies (Eberhart-Phillips and Michael, 1993; Shapiro et al., 2005; Thurber et al., 2006). The utility of geophysical explorations has been demonstrated for studies of local fault structure (Griscom and Jachens, 1990; Unsworth et al., 1997; McPhee et al., 2004; Le Pichon et al., 2005; Fialko, 2006; Wdowinski et al., 2007). Detailed fault structure can be imaged well by combining methods based on multiple approaches (Unsworth et al., 1997; Fuis et al., 2012).

Drilling may be the most direct method to study fault-zone properties. However, it is applicable only in limited situations (Zoback et al., 2010). Fault-zone head waves and guided waves are influenced by fault-zone properties, which enable us to infer the physical properties of the medium (Ben-Zion and Malin, 1991; Hough et al., 1994; Korneev et al., 2003; Lewis et al., 2007; Zhao and Peng, 2008; Zhao et al., 2010). The spatial distribution of seismicity may be useful as an indirect method for making inference regarding fault geometry (Eberhart-Phillips and Michael, 1993; Thurber et al., 2006).

Accurate determination of event locations may be essential for the elucidation of fault geometry using seismicity. A number of hypocentral-inversion methods including HYPO71 (Lee and Lahr, 1975; Lee, 1990), HYPOINVERSE (Klein, 1978, 2002), HYPOELLIPSE (Lahr, 1980), VELEST (Kissling et al., 1994), HYPOSAT (Schweitzer, 1997), and HYPODD (Waldhauser and Ellsworth, 2000) have been proposed. In particular, a double-difference location technique (e.g., HYPODD) has been determined found to be useful for clustered events (Waldhauser et al., 2004). However, the hypocentral parameters obtained using such methods are highly influenced by the accuracy of the implemented velocity models (Kim et al., 2014). This feature makes it difficult to apply such 1-D velocity-model-based methods to seismicity in regions with complex velocity structures.

Fault zone structures are naturally complex, and they are poorly represented by 1-D velocity models (Kim et al., 2014). Attempts have been made to perform hypocentral-parameter inversions based on 3-D velocity models (e.g., Thurber et al., 2006). However, fine-scale structures can be represented only limitedly even with 3-D velocity models. An inversion based on adaptive velocity models may be desirable for correct determination of hypocentral parameters of events in complex-

* Corresponding author.
E-mail addresses: wookim@gnu.ac.kr (W. Kim), tkhong@yonsei.ac.kr (T.-K. Hong), aqualung@yonsei.ac.kr (J. Lee), taira@berkeley.edu (T. Taira).

http://dx.doi.org/10.1016/j.tecto.2016.03.038

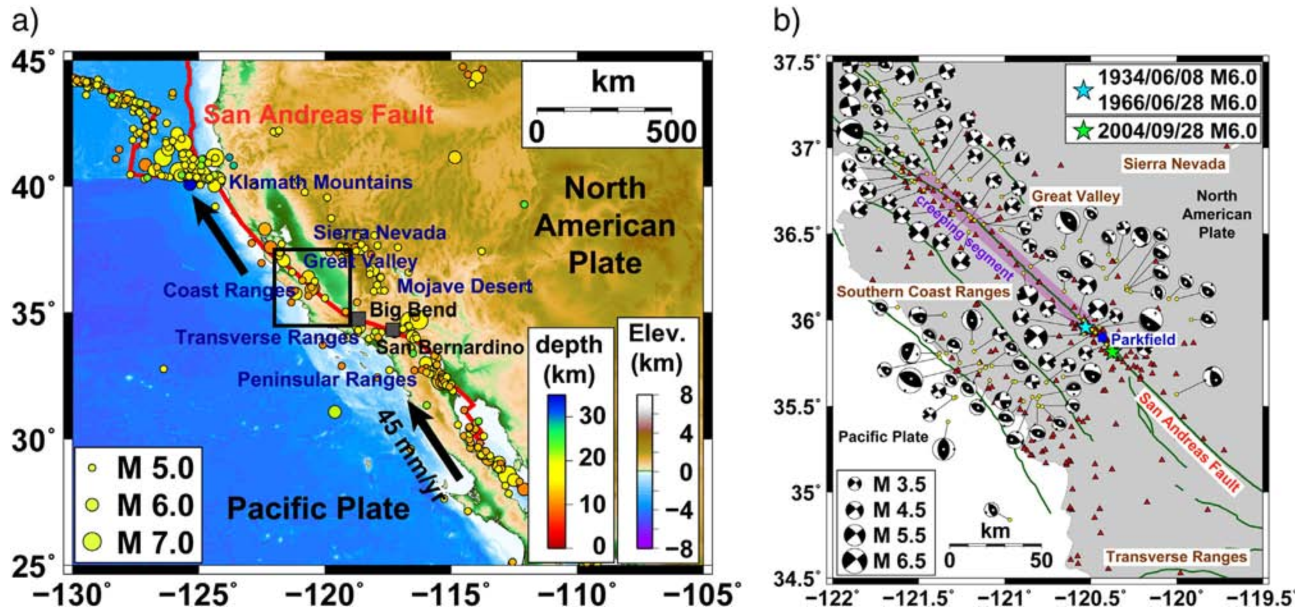

Fig. 1. (a) Tectonic setting around the western North American plate. The study region is marked with a black box. Major events with magnitudes greater than or equal to 5 are presented (circles). (b) Enlarged map of the study region around Parkfield with the focal mechanism solutions of major earthquakes (Ekström et al., 2012). Major geological structures are denoted. Stations (triangles) are distributed densely around the faults. The epicenters of periodic M6 events are marked (stars).

velocity regions (Lees and Malin, 1990; Michelini and McEvilly, 1991; Eberhart-Phillips and Michael, 1993; Thurber et al., 2003, 2004, 2006; Lin et al., 2010).

Seismicity is naturally associated with faulting. Microearthquakes may occur in local branches around a major fault, resulting in a complex distribution of seismicity. Seismicity of several or more years is expected to present the dominant seismic activity in the fault system. Seismicity is useful to constrain fault geometry, which provides important information for assessing potential seismic hazards. In this study, we investigate the seismicity around the San Andreas fault (SAF) in central California. The hypocentral parameters of the earthquakes are determined using a hypocentral-parameter inversion method based on an adaptive-velocity-model-updating scheme. The inverted hypocenters are compared with those obtained using other conventional methods. The fault dips and the geometry along the fault trace are investigated using the vertical distribution of seismicity.

2. Geology and tectonics

The San Andreas fault (SAF) is an approximately 1100-km-long right-lateral strike-slip fault that forms a plate boundary between the Pacific and North American plates along the west coast of the US (Catchings et al., 2002; Fig. 1). The locking segments of the SAF are separated by a 175-km-long creeping segment in central California (Harris and Segall, 1987; Nadeau and McEvilly, 2004). The fault naturally divides the basements of the Pacific and North American plates. The southwestern basement is formed of Salinian granite overlain by Quaternary and Tertiary sediments (Dibblee, 1980; Unsworth et al., 1997). The northeastern basement contains a melange of metamorphosed accretionary prism overlain by Tertiary and Holocene sediments.

The slip rates on the locked segment in northern California are 13–22 mm/yr, and those on the locked segment in southern California are 12–22 mm/yr (Geist and Andrews, 2000; Behr et al., 2010). In contrast,

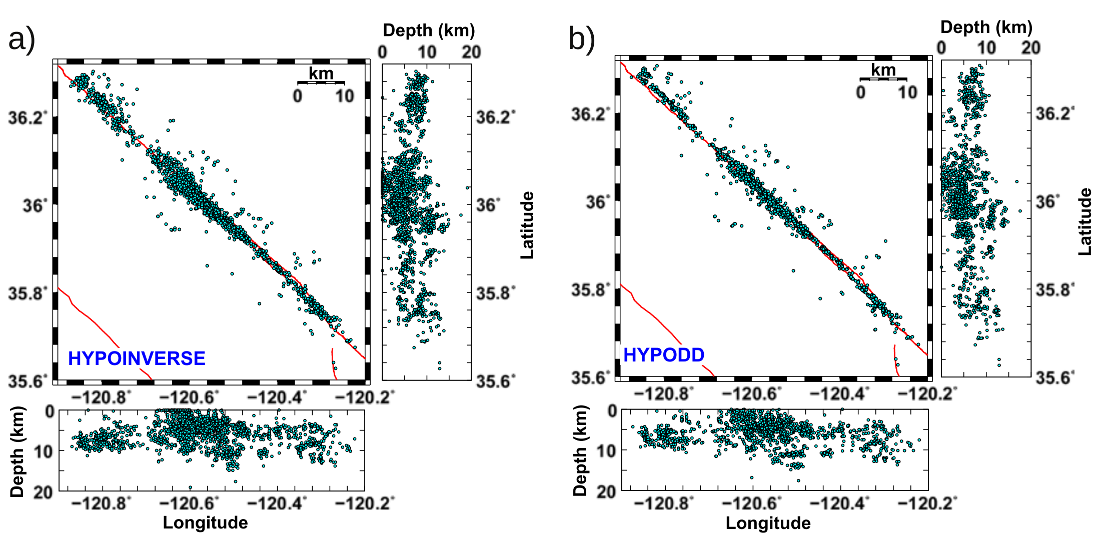

Fig. 2. Event epicenters and focal depths determined by (a) HYPOINVERSE and (b) HYPODD. The epicenters from HYPOINVERSE are diffused around the fault trace, whereas those from HYPODD are clustered along the fault trace. Most focal depths are less than 15 km.

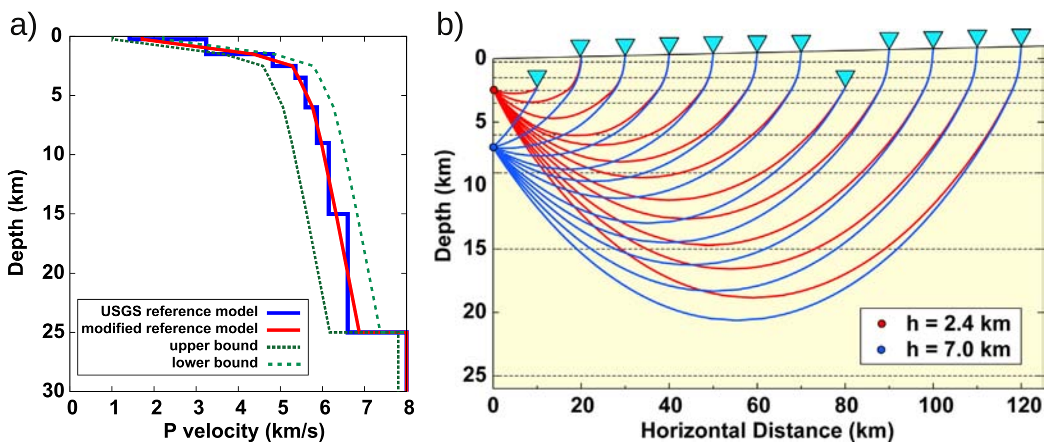

Fig. 3. (a) *P* velocity models for hypocentral-parameter inversion. A modified 1-D reference velocity model is designed after the USGS velocity model (Klein, 2002). The optimum velocity model is determined between the upper and lower bounds of velocity ranges. (b) An example of ray tracing for a medium with surface topography varying up to 1 km above sea level. Two events at depths of 2.4 and 7.0 km are considered. Stations are placed with a uniform inter-station interval of 10 km for epicentral distances of 0 to 120 km.

the slip rates on the creeping segment in central California are as high as ~30 mm/yr (Burford and Hash, 1980; Titus et al., 2006).

Right-lateral strike-slip earthquakes are dominant along the SAF (Thurber et al., 2006). Reverse earthquakes occur in regions off the San Andreas fault zone in central California (Fig. 1). Two major earthquakes have occurred in the locked segments of the SAF since 1800 (Sieh, 1978; Titus et al., 2006). The 1857 M_w7.9 Fort Tajon earthquake ruptured the southeastern locked segment (Sieh, 1978). The 1906 M_w7.9 San Francisco earthquake occurred in the northwestern locked segment, producing a coseismic slip of 4–5 m over a rupture plane of ~500 km (Thatcher et al., 1997; Aagaard et al., 2008).

It is noteworthy that moderate earthquakes occur regularly in the Parkfield fault zone. Six M6 earthquakes have occurred since 1857 in the Parkfield fault zone (Bakun and Lindh, 1985; Unsworth et al., 1997; Bakun et al., 2005). The M6 earthquakes in 1934 and 1966 occurred in the northern margin of the southwestern locking segment on a fault plane with a strike of N39 °W and a dip of 86 °SW (Eaton et al., 1970; Trifunac and Udwadia, 1974). The most recent periodic M6 earthquake occurred on 28 September 2004 on a fault plane with a strike of N40 °W and a dip of 87 °SW, and was located at ~21.4 km SW from the epicenters of the preceding M6 earthquakes of 1934 and 1966 (Custódio et al., 2005; Liu et al., 2006; Kim and Dreger, 2008).

The dipping angle of the SAF in northern California has been reported to be nearly vertical in the seismogenic depth range (up to 12 km) and 60 °NE–70 °NE up to the Moho (Parsons and Hart, 1999). On the other hand, the dipping angle of the SAF through the Transverse Ranges in southern California varies spatially. The dipping angles are 55 °SW in Big Bend, near-vertical in the Mojave desert, 37 °NE in San Bernardino, 52 °NE in North Palm Springs, and 65 °NE in Indio (Fuis et al., 2012).

3. Data

We collect arrival-time information of 2388 earthquakes in the central segment of the SAF during 2001–2002 and 2010–2012. The event magnitudes are −0.2 to 4.4. We analyze 2112 events for which hypocentral parameters from HYPODD and HYPOINVERSE are available (Fig. 2). The source parameters estimated by HYPODD and HYPOINVERSE are obtained from the event catalogs of Northern California Earthquake Data Center (NCEDC) and available resources (Thurber et al., 2003; Waldhauser et al., 2004). The focal depths are found to be lower than 20 km (Fig. 2).

The onset times of local *P* waves are identified well, whereas *S* waves are naturally contaminated by *P* coda. Thus, the arrival times of *S* waves have larger errors than those of *P* waves. In this study, the hypocentral parameter inversions are made on the basis of only the *P* arrival times to decrease the error in analysis. The arrival times of *P* waves at 280 local stations are collected from the earthquake catalog of the Northern California Seismic Network (NCEDC, 2014; Fig. 1). We refine the hypocentral parameters of events with *P* arrival times at eight or more stations.

4. Methods

The hypocentral parameters from conventional inversion methods are influenced by the implemented velocity models. The conventional

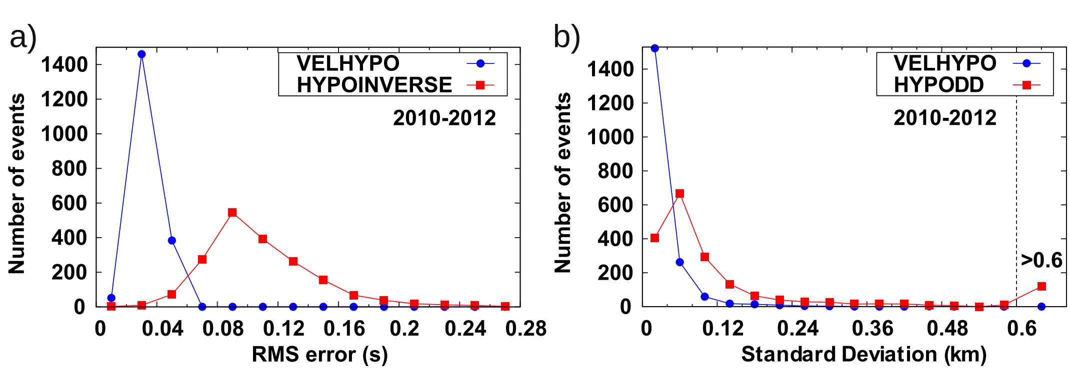

Fig. 4. Comparisons of (a) root-mean-squares (RMS) errors of traveltimes between HYPOINVERSE and VELHYPO and (b) standard deviations of hypocenters between HYPODD and VELHYPO for the data set analyzed in this study. The hypocentral-parameter estimates from VELHYPO display higher accuracy than those obtained from other conventional methods (HYPOINVERSE, HYPODD) based on 1-D seismic velocity models.

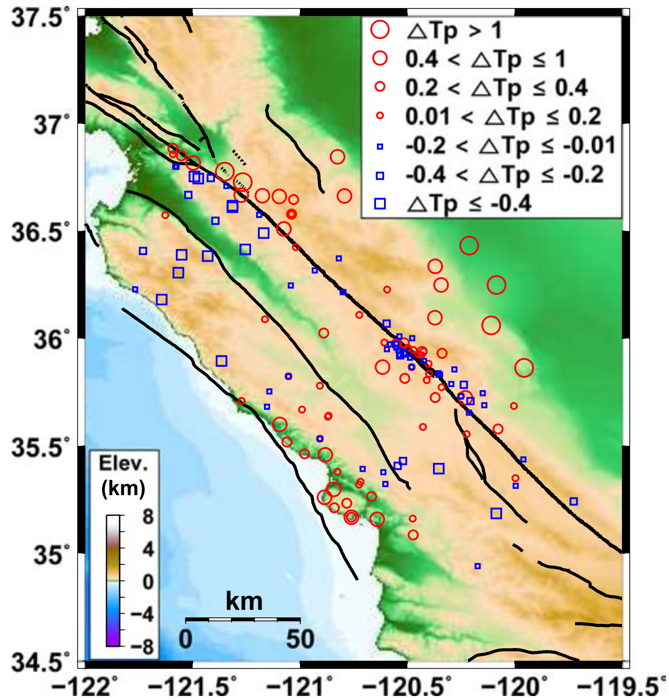

Fig. 5. Station correction terms for P travel times (ΔT_P) determined from the hypocentral-parameter inversions, suggesting regional seismic velocity anomalies. Positive station correction values (lower seismic velocities) are observed in the region east of the fault, with negative station correction values (higher seismic velocities) in the region to the west. Localized low velocity anomalies are observed around the southwestern coast.

hypocentral-parameter inversion methods based on fixed 1-D velocity models may yield errors in the inverted hypocentral parameters of events in laterally-varying velocity structures (Kim et al., 2014). The medium of a fault zone is laterally heterogeneous, causing poor representation of the medium with a 1-D velocity model. It has been reported that hypocentral inversion methods based on adaptive velocity models (e.g., GA-MHYPO, VELHYPO) are useful for events in complex media (Kim et al., 2014). The VELHYPO method searches the adaptive 1-D optimum velocity model with an iterative velocity-updating scheme (Kim et al., 2014).

We construct a reference 1-D velocity model in which the velocity increases linearly with depth:

$$v_i^r(z) = a_i z + b_i, \tag{1}$$

where v_i^r is the reference velocity of the i-th layer, z is the depth, and a_i and b_i are constants. This linear velocity model yields an environment where crustally-refracted waves (head waves) are not observed as the first arrival phase. An optimum velocity model is searched among a set of 1-D velocity models that are prepared by adding constants within a prescribed range to the reference linear velocity model (Fig. 3). The prescribed range is set to be ± 0.55 km/s considering possible velocity variations in the region (e.g., Thurber et al., 2003). The constant for the optimum velocity model corresponds to the average-velocity residual between the target medium and reference model. A positive velocity residual suggests that the average velocity of the target medium is higher than that of the implemented reference velocity model.

The optimum velocity model is determined to have the minimum misfit errors in traveltimes and locations. The misfit function, F, is designed to combine the traveltime and focal depth errors, which was

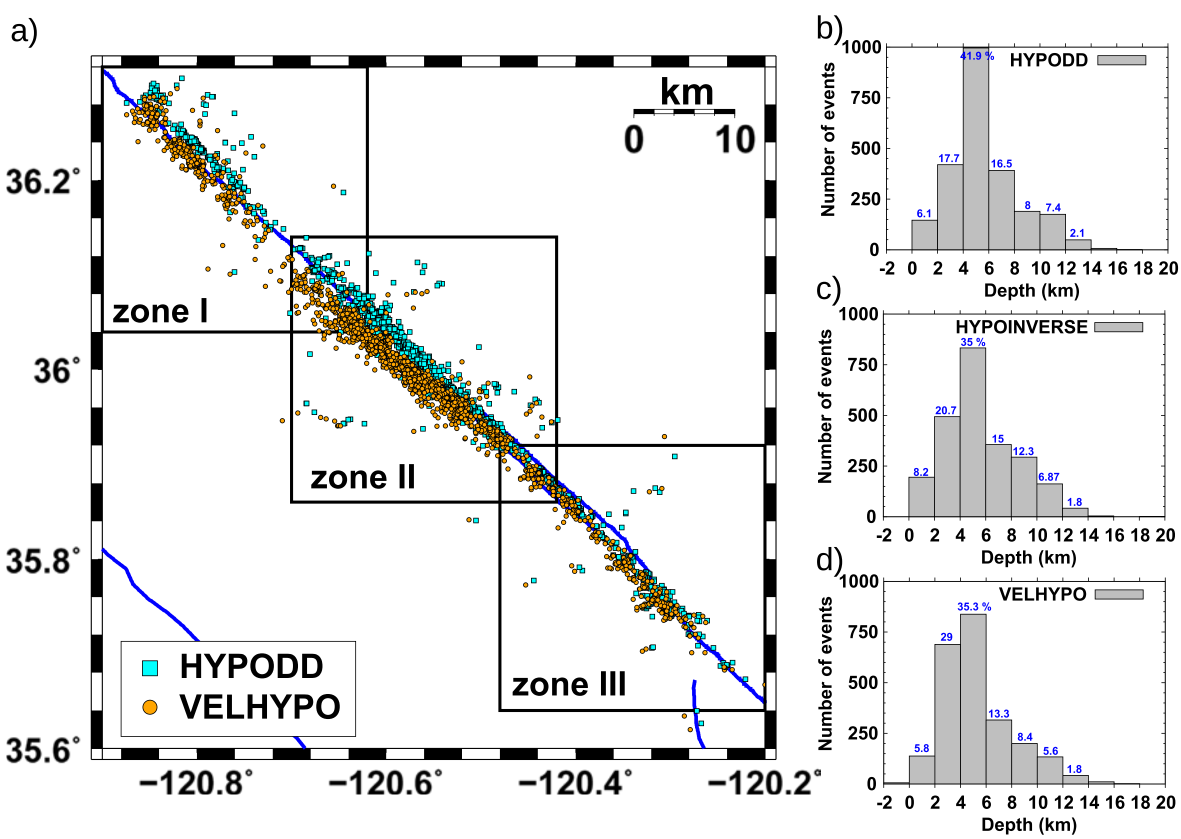

Fig. 6. (a) Spatial distribution of event epicenters determined by VELHYPO. The epicenters from HYPODD are presented for comparison. The epicenters from VELHYPO are generally located in the region to the west of the fault, which is a different result from those obtained using other methods. The region is divided into three subregions (zones I, II, III) for comparison of every epicenter. Histograms of focal-depth distribution for hypocentral parameters from (a) HYPODD, (b) HYPOINVERSE and (c) VELHYPO. The relative population of events at each depth range is presented. About ~91% of earthquakes occur at depths less than 10 km.

found to be useful for stable inversion (Kim et al., 2006, 2014):

$$F = \sqrt{\frac{\sum_{j=1}^{n} w_j \Delta t_j^2}{\sum_{j=1}^{n} w_j} + \frac{\sigma_z}{v_a}}, \tag{2}$$

where n is the number of stations, w_i is the weighting factor, Δt_i is the root-mean-squares (RMS) traveltime residual of P waves at station j, σ_z is the standard deviation of focal depth estimates, and v_a is a given reference velocity.

Once the hypocentral parameters and an optimum velocity model are determined, station correction terms are estimated from the resultant traveltime differences. Here, the possible presence of systematic errors in traveltime data for a certain event can be examined from the average traveltime residuals of all stations. The station correction term for a certain station is calculated by averaging the traveltime residuals at the station for all observed events. The traveltime residuals and station correction terms are calculated at every iteration of the hypocentral-parameter inversion. The hypocentral parameters and optimum velocity models are refined iteratively.

The 1-D optimum velocity model is determined for every event-station pair. The weighted average velocity of the optimum velocity model is expected to coincide with that of the actual structure (Kim et al., 2014). The optimum velocity model enables us to infer the 3-D velocity perturbation. This feature suggests the effectiveness of VELHYPO for hypocentral parameter inversion of events in regions with poorly-constrained velocity structures.

In this study, the raypaths between events and stations are calculated using a high-accuracy two-point ray tracing algorithm (Kim and Baag, 2002). The location error associated with ray tracing generally decreases with iterative number (Fig. 3). The ray-tracing algorithm can be applied to media with surface topography (Kim and Baag, 2002).

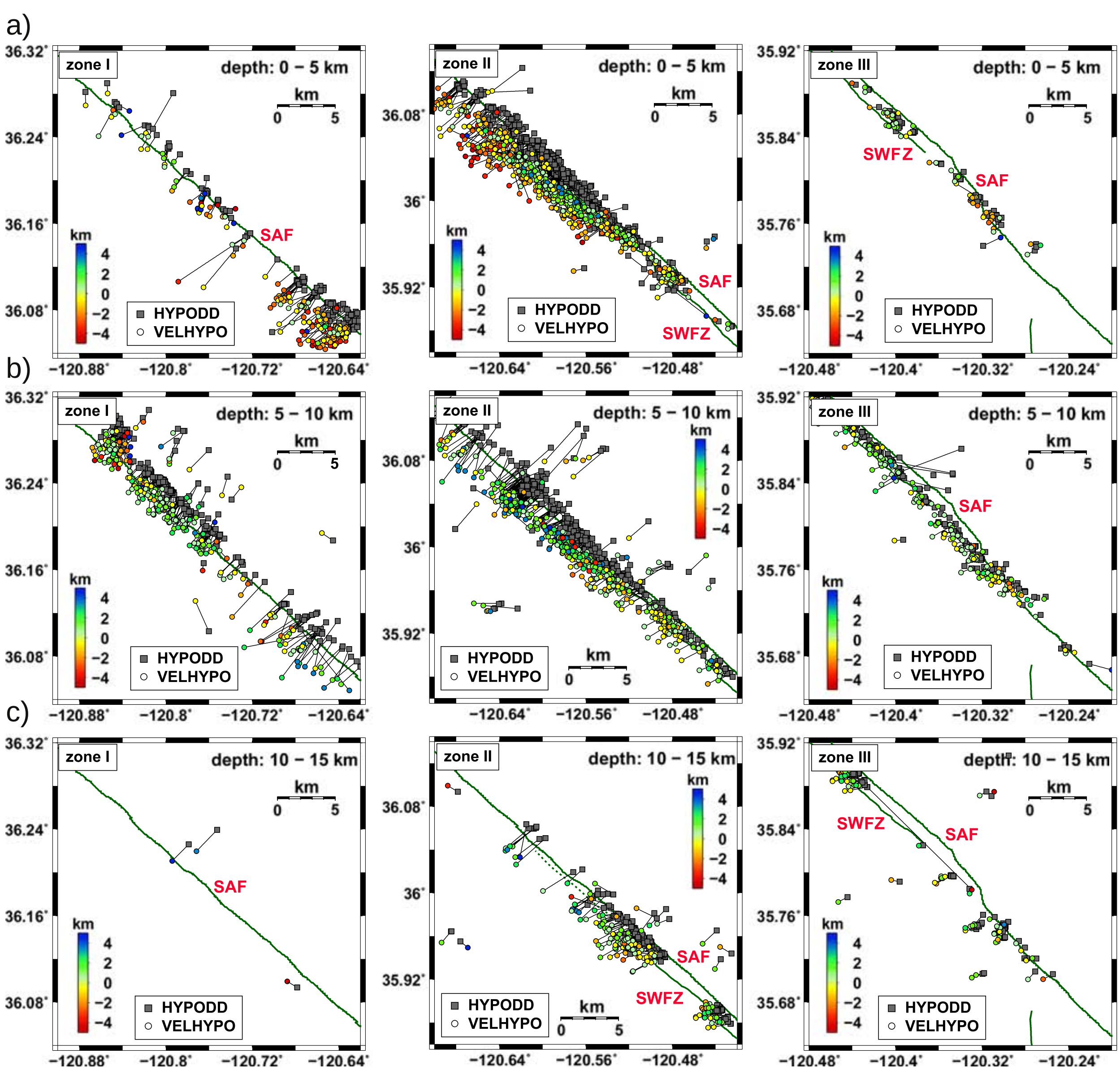

Fig. 7. Distribution of hypocenters from VELHYPO with respect to those from HYPODD in three subregions (zones I, II, and III) at three depth ranges: (a) 0–5 km, (b) 5–10 km, and (c) 10–15 km. The hypocenters are generally dislocated up to 5 km SW (fault-normal direction) from those of HYPODD. Positive focal-depth changes indicate increased focal depths, while negative focal-depth changes represent decreased focal depths. The focal depths obtained from VELHYPO are generally greater than those from HYPODD in shallow depths (0–5 km) of zones I and II. Positive and negative changes of focal depths are mixed in the other zones and depths. The San Andreas fault (SAF) and Southwest Fracture Zone (SWFZ) are marked.

5. Analysis

The hypocentral parameters of earthquakes are inverted using VELHYPO based on *P* arrival times. Events with eight or more *P* arrival times are analyzed. The average number of *P* arrival times is about 20. The hypocentral parameters (origin time, epicentral location, and focal depth) are determined tentatively in the first round of inversion based on all available *P* arrival times. The hypocentral parameters are refined using a selected data set of *P* arrival times for stations with epicentral distances less than 10 times the focal depths. The epicentral distances are less than 80 km.

The reference *P*-velocity model is constructed by modifying the 1-D velocity model of the United States Geological Survey (USGS), which consists of nine crustal layers (Klein, 2002). The boundaries between the layers are located at depths of 0.25, 1.5, 2.5, 3.5, 6, 9, and 15 km (Fig. 3). The Moho in the model is placed at a depth of 25 km. The seismic velocities in the first and second layers are set to be slightly higher than those of the USGS velocity model to avoid possible traveltime triplications in local distances. In addition, the seismic velocities in each layer increase linearly with depth. In this model, waves along the direct path between an event with a focal depth of 2.4 km and a station on the surface are the first-arrival phase in an epicentral distance less than 5 km. On the other hand, the direct waves from an event with a focal depth of 7.0 km arrive first in an epicentral distance less than 30 km (Fig. 3(b)).

The RMS traveltime errors of the relocated earthquakes are less than 0.07 s, and the standard deviations of hypocenters are less than 0.12 km for 99% of data (Fig. 4). The conventional methods (HYPOINVERSE, HYPODD) yield much larger RMS traveltime errors and standard deviations of hypocenters compared to those of VELHYPO (Fig. 4). We select data with RMS traveltime errors less than 0.05 s and location standard deviations less than 0.05 km to improve the stability of inversion.

The optimum velocity models represent the seismic velocities along the raypaths. The differences between the optimum velocity models reflect the relative velocity perturbations between the raypaths. The average of optimum velocity models for raypaths from a certain station to spatially-distributed events presents the velocity perturbation in the medium beneath the station. The station correction terms are determined from the traveltime residuals.

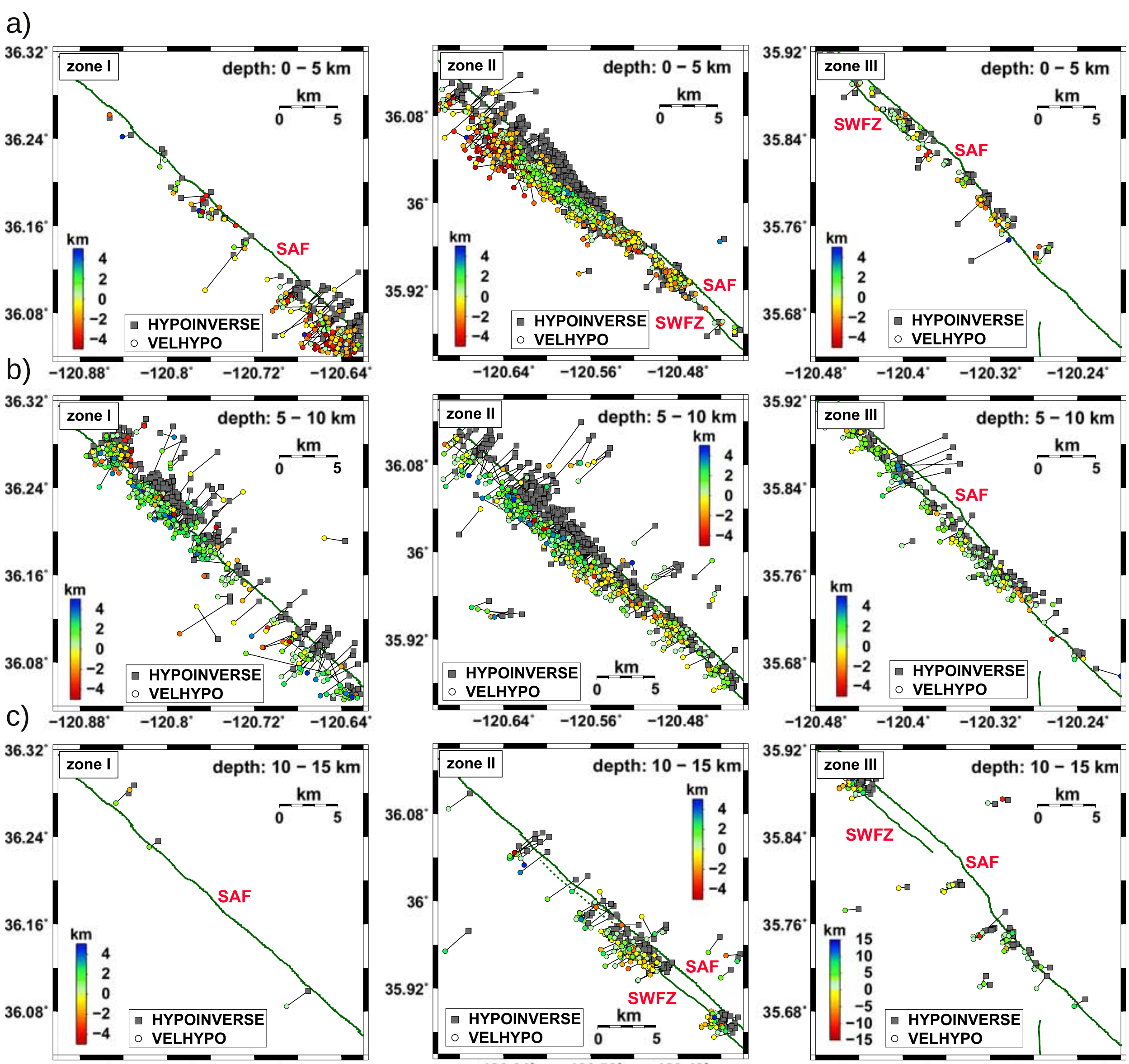

Fig. 8. Distribution of hypocenters from VELHYPO with respect to those from HYPOINVERSE for three subregions (zones I, II, and III) at three depth ranges: (a) 0–5 km, (b) 5–10 km, and (c) 10–15 km. The hypocenters are generally dislocated up to 5 km SW (fault-normal direction) from those of HYPOINVERSE. Positive focal-depth changes represent increased focal depths, while negative focal-depth changes indicate decreased focal depths. The general features of focal-depth changes are similar to those observed in Fig. 7.

Positive station correction terms (low velocity anomalies) are found in the region east of the fault, with negative station correction terms (high velocity anomalies) in the region to the west (Fig. 5). Also, positive station correction terms are observed in the southwest region along the west coast. The spatial distribution of station correction terms suggests lateral variation of velocity structures around the fault zone, which is consistent with the observations of seismic tomography studies (e.g., Shapiro et al., 2005). The spatial variation of station correction terms supports the accuracy of the inverted source parameters.

6. Refined seismicity

The hypocenters determined by VELHYPO are presented in Fig. 6. The refined seismicity is clustered around the northwestern zone of the creeping segment. On the other hand, earthquakes rarely occur in the southeastern zone in the locked segment. The observation is consistent with the relocated seismicity based on a 3-D velocity model (Bakun et al., 2005; Thurber et al., 2006). It is observed that ~91% of earthquakes are located at depths less than 10 km (Fig. 6). Also, earthquakes are most populated (~64% of events) in the depth range of 2–6 km. The study region is divided into three subregions (zones I, II, and III) for comparison of hypocenters in three depth ranges (0–5, 5–10, and 10–15 km) between the three methods (HYPODD, HYPOINVERSE, and VELHYPO) (Figs. 7, 8).

The epicenters of HYPODD and HYPOINVERSE are generally clustered around the fault trace on the surface. The epicenters determined by VELHYPO are located at 1.78 ± 1.69 km SW in zone I, 1.39 ± 1.20 km SW in zone II, and 0.44 ± 0.56 km SW in zone III with respect to those of HYPODD for events at depths of 0–5 km (Fig. 9). Similar features are observed for events at deeper depths (5–10, and 10–15 km). We find that the epicenters from VELHYPO are located at 0.4–2.0 km SW on average from those from HYPODD at all zones and depths. The focal depths determined by VELHYPO are larger by 1.68 ± 1.90 km in zone I, 0.03 ± 1.68 km in zone II and 0.38 ± 1.68 km in zone III than those determined by HYPODD for events at depths of 0–5 km. However, the focal depths from VELHYPO are shallower on average than those from HYPODD in the other depth ranges (5–10, and

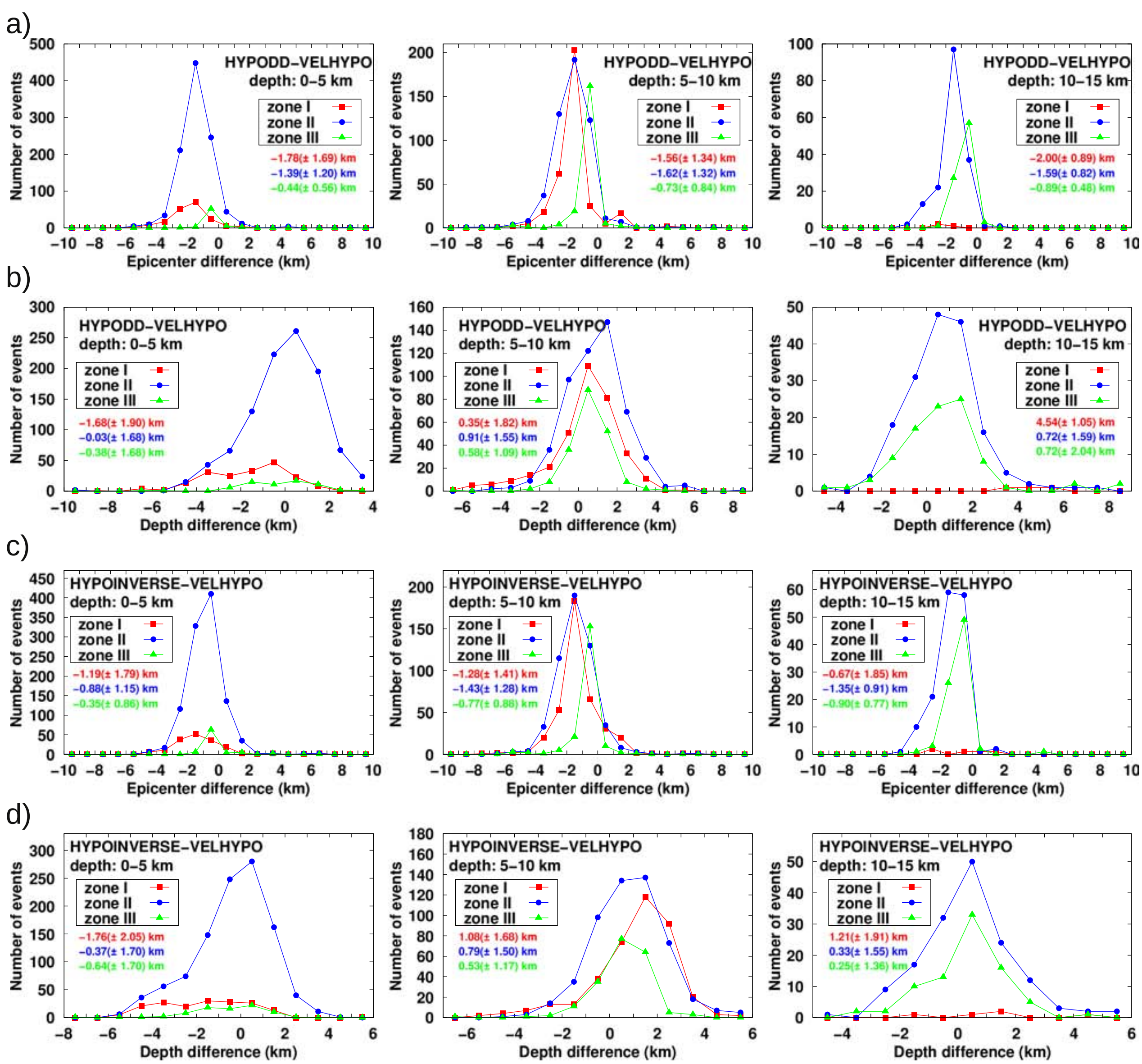

Fig. 9. Comparisons of (a) epicenter differences and (b) focal-depth differences between HYPODD and VELHYPO, and (c) epicenter differences and (d) focal depth differences between HYPOINVERSE and VELHYPO. Negative values of epicenter differences suggest that the epicenters from VELHYPO are located further to the west than those from the counterpart methods (HYPODD, HYPOINVERSE). Negative values of focal-depth differences suggest that the focal depths from VELHYPO are shallower than those obtained using other methods. The epicenters from VELHYPO are located 0.4–2.0 km SW from those determined by other methods. The focal-depth differences are mixed.

10–15 km). We find similar features of epicenter and focal-depth differences between VELHYPO and HYPOINVERSE (Fig. 9). The epicenters from VELHYPO are particularly clustered around the surface trace of the SAF in zone I and the Southwest Fracture Zone (SWFZ) in zones II and III.

The epicenter differences between VELHYPO and other methods are in good agreement with the lateral velocity variation around the fault zone in Fig. 5, which is consistent with 3-D velocity models (e.g., Thurber et al., 2006). The characteristic hypocenter differences between VELHYPO and other methods may be partly associated with the accuracy of implemented 1-D velocity models that may not be good enough to represent the laterally-varying velocity structures in fault zones. The two conventional methods (HYPODD, HYPOINVERSE) are based on a constant 1-D velocity model, whereas VELHYPO implements an adaptive 1-D velocity model that searches an optimum velocity model for each raypath. The adaptive 1-D velocity models may represent the 3-D velocity heterogeneities along raypaths reasonably well.

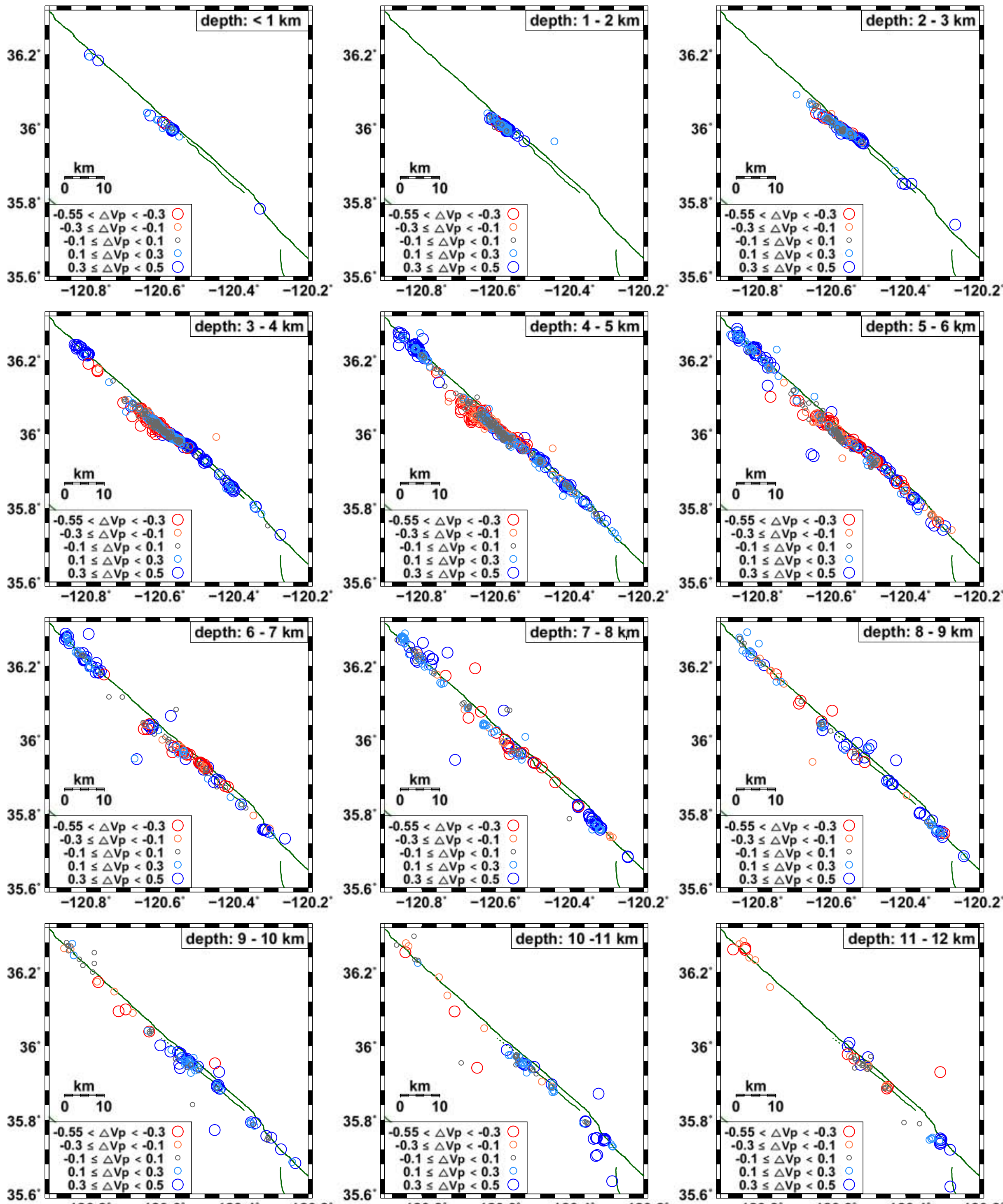

Fig. 10. Lateral variation of velocity residuals at the event hypocenters. High seismic velocity anomalies are observed at shallow depths. Low seismic velocity anomalies are observed at depths of 3–8 km in the central fault zone, and high seismic velocity anomalies are present in the northern and southern fault zones. Low seismic velocities are observed in the northern fault zone at depths deeper than 8 km.

7. Seismic velocity structure along the fault

The optimum velocity model is determined for each source-receiver pair. The velocity residuals of optimum velocity models with respect to the reference velocity model are stacked for common events to assess the seismic velocities in the media around the sources (Fig. 10). Seismic velocities are generally high at depths less than 3 km along the fault. Seismic velocities at depths of 3–8 km are observed to be low in the central fault zone, and high in the northwestern and southeastern fault zones. Seismic velocities at depths greater than 8 km are low in the northeastern fault zone, but high in the southeastern fault zone. In general, the northwestern and southeastern fault zones display higher seismic velocities, whereas the central fault zone presents lower seismic velocities.

It is noteworthy that dip-slip events occur in the central Parkfield fault zone where low seismic velocities are observed (Fig. 1). The occurrence of events with a unique focal mechanism may be a consequence of local perturbations of the ambient stress field and medium properties. This observation suggests possible complexity of fault geometry.

8. Fault geometry

The hypocenter distribution on fault-normal cross sections illuminates the fault geometry. The fault zone is divided into 8 subregions

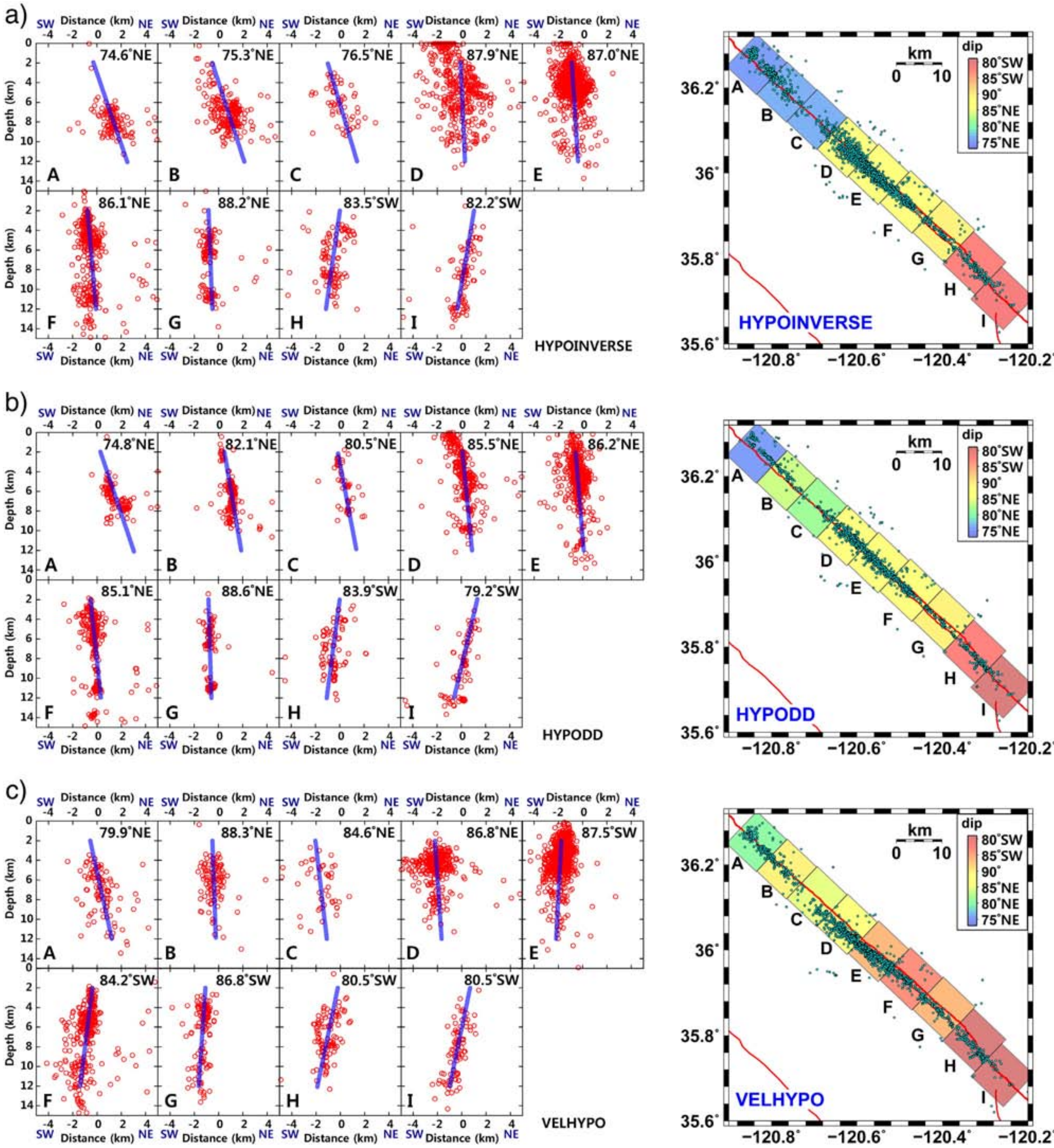

Fig. 11. Determination of fault-plane dips based on the vertical distribution of hypocenters from (a) HYPOINVERSE, (b) HYPODD, and (c) VELHYPO. The vertical distribution of seismicity suggests that the fault dips NE in the northwestern region, nearly vertical in the central region, and SW in the southeastern region.

with a size of 10 km-by-10 km along the fault trace on the surface. The dip of a fault segment is determined from the vertical hypocenter distribution of events on cross sections using a least squares fitting (Fig. 11). The hypocenters of events at depths of 2–12 km are used considering the seismogenic depths of the region and possible bending of the fault plane near the surface (Parsons and Hart, 1999; Hole et al., 2006). The vertical hypocenter distribution and fault-plane dips are compared between three hypocentral-inversion methods (HYPODD, HYPOINVERSE, and VELHYPO).

The hypocenters from all three methods generally illuminates NE-directional fault-plane dipping in the northwestern zone, near-vertical dipping in the central segment, and SW-directional dipping in the southeastern zone (Fig. 11). The dipping angles change gradually with distance, forming a 3-D spiral geometry (Fig. 12). This general feature agrees with early studies of seismic velocity structures (Simpson et al., 2006; Thurber et al., 2006), gravity and magnetic anomalies (Griscom and Jachens, 1990), and drilling observations (Zoback et al., 2010).

The dipping angles illuminated by the hypocenters from HYPOINVERSE are determined to be 74.6 °NE (zone A) to 82.2 °SW (zone I). On the other hand, the fault dips from the hypocenter estimates of HYPODD are determined to be 74.8 °NE (zone A) to 79.2 °SW (zone I). The hypocenters from VELHYPO suggest the dipping angles to be between 79.9 °NE (zone A) and 80.5 °SW (zone I).

The hypocenter data from HYPOINVERSE and HYPODD suggest the presence of a near-vertical fault plane at the location around (120.35 °W, 35.85 °N), whereas those from VELHYPO indicate such a fault plane at the location around (120.55 °W, 36.05 °N). The near-vertical fault plane inferred from the hypocenters of VELHYPO is located NW of those from HYPOINVERSE and HYPODD. It is observed that the near-vertical fault plane is located in a region of low seismic velocities (Fig. 10). Also, high seismicity is observed in the SWFZ which developed beside the creeping segment of the SAF. The dominant seismicity beneath the SWFZ suggests the development of local active faults.

9. Discussion and conclusions

The hypocenters of earthquakes in the Parkfield fault zone are refined using an adaptive-velocity-based hypocentral-parameter inversion method. The implemented method has high accuracy compared to conventional methods based on a 1-D velocity model. It was observed that the RMS traveltime errors were less than 0.07 s in 99% of the data, and the standard deviations of hypocenters were less than 0.12 km. The conventional methods (HYPOINVERSE, HYPODD) presented larger RMS traveltime errors and standard deviations of hypocenters.

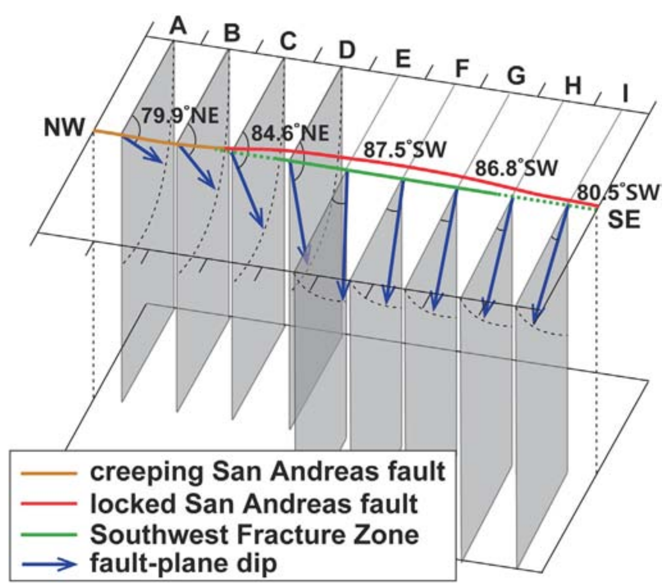

Fig. 12. A schematic model of fault-plane dipping angles (arrows) in Parkfield, presenting an apparent spiral geometry. Earthquakes in regions A and B occur in the creeping northwestern SAF that dips NE. The earthquakes in regions C and D are scattered around the SAF and the SWFZ, dipping NE at higher angles. The earthquakes in regions E to I mainly occur in the SWFZ, dipping near-vertically and SW.

The epicenters determined in this study were located on average 0.4–2.0 km SW of those determined by conventional hypocentral methods based on a fixed 1-D velocity model. The station correction terms from the hypocentral-parameter inversion suggest characteristic regional variation of seismic velocities around the fault that is consistent with seismic tomography studies (Shapiro et al., 2005). The seismic velocity residuals stacked for common events produce the seismic velocities in the source regions, displaying systematic low velocities in the central fault zone and high seismic velocities in the northwestern and southeastern fault zones.

The refined seismicity is observed to be clustered in the Southwest Fracture Zone, which has developed beside the creeping segment of the SAF. On the other hand, the number of earthquakes decreases in the southeastern locked segment. The vertical distribution of seismicity suggests an apparent spiral geometry of the fault plane, dipping NE in the northwestern zone, nearly vertical in the central zone, and SW in the southeastern zone. The fault dips are determined to vary between 79.9 °NE and 80.5 °SW. Fault geometry changes markedly within a distance of ~50 km. The lateral variation of seismic velocities and spiral fault geometry cause a localized concentration of tectonic-loading stress, which may cause the periodic M6 earthquakes in the Parkfield region.

Acknowledgments

We thank Felix Waldhauser for valuable comments on the seismicity and fault system in Parkfield. We thank Dr. Guillermo Booth Rea (editor) and two anonymous reviewers for fruitful comments that improved the presentation of the manuscript. This work was supported by the Korea Meteorological Administration Research and Development Program under Grant KMIPA 2015-7040. TT was partly supported by the National Science Foundation EAR-0910322. Waveform data, metadata, and earthquake catalog for this study were accessed through the Northern California Earthquake Data Center (NCEDC) (NCEDC, 2014).

References

Aagaard, B.T., Brocher, T.M., Dolenc, d., Dreger, D., Graves, R.W., Harmsen, S., Hartzell, S., Larsen, S., McCandless, K., Nilsson, S., Petersson, N.A., Rodgers, A., Sjogreen, B., Zoback, M.L., 2008. Ground-motion modeling of the 1906 San Francisco earthquake, part II: ground-motion estimates for the 1906 earthquake and scenario events. Bull. Seismol. Soc. Am. 98 (2), 1012–1046.

Bakun, W.H., Lindh, A.G., 1985. The Parkfield, California, earthquake prediction experiment. Science 229 (4714), 619–624.

Bakun, W.H., Aagaard, B., Dost, B., Ellsworth, W.L., Hardebeck, J.L., Harris, R.A., Ji, C., Johnston, M.J.S., Langbein, J., Lienkaemper, J.J., Michael, A.J., Murray, J.R., Nadeau, R.M., Reasenberg, P.A., Reichle, M.S., Roeloffs, E.A., Shakal, A., Simpson, R.W., Waldhauser, F., 2005. Implications for prediction and hazard assessment from the 2004 Parkfield earthquake. Nature 437, 969–974.

Behr, W.M., Rood, D.H., Fletcher, K.E., Guzman, N., Finkel, R., Hanks, T.C., Hudnut, K.W., Kendrick, K.J., Platt, J.P., Sharp, W.D., Weldon, R.J., Yule, J.D., 2010. Uncertainties in slip-rate estimates for the Mission Creek strand of the southern San Andreas fault at Biskra Palms Oasis, southern California. Geol. Soc. Am. Bull. 122 (9-10), 1360–1377.

Ben-Zion, Y., Malin, P., 1991. San Andreas fault zone head waves near Parkfield. Calif. Sci. 251, 1592–1594.

Burford, R.O., Hash, P.W., 1980. Slip on the San Andreas fault central California from aliment array survey. Bull. Seismol. Soc. Am. 70, 1233–1261.

Catchings, R.D., Rymer, M.J., Goldman, M.R., Hole, J.A., Huggins, R., Lippus, R., 2002. High-resolution seismic velocities and shallow structure of the San Andreas fault zone at Middle Mountain, Parkfield, California. Bull. Seismol. Soc. Am. 92, 2493–2503.

Custódio, S., Liu, P., Archuleta, R.J., 2005. The 2004 Mw6.0 Parkfield, California, earthquake: inversion of near-source ground motion using multiple data set. Geophys. Res. Lett. 32, L23312 doi:10.1029/2005GL024417.

Dibblee, T.R., 1980. Geology along the San Andreas fault from Gilroy to Parkfield, in studies of the San Andreas fault zone in northern California. In: Streitz, R., Sherburne, R. (Eds.), California Division of Mines and Geology, Special Report 140, pp. 3–18 Sacramento.

Eaton, J.P., O'Neill, M.E., Murdock, J.N., 1970. Aftershocks of the 1966 Parkfield-Cholame, California, earthquake: a detailed study. Bull. Seismol. Soc. Am. 60 (4), 1151–1197.
Eberhart-Phillips, D., Michael, A.J., 1993. Three-dimensional velocity structure, seismicity, and fault structure in the Parkfield region, central California. J. Geophys. Res. 98, 15,737–15,758.
Ekström, G., Nettles, M., Dziewonski, A.M., 2012. The global CMT project 2004–2010: centroid-moment tensors for 13,017 earthquakes. Phys. Earth Planet. Inter. 200-201, 1–9.
Fialko, Y., 2006. Interseismic strain accumulation and the earthquake potential on the southern San Andreas fault system. Nature 441, 968–971.
Fuis, G.S., Ryberg, T., Godfrey, N.J., Okaya, D.A., Murphy, J.M., 2001. Crustal structure and tectonics from the Los Angeles basin to the Mojave Desert, southern California. Geology 29, 15–18.
Fuis, G.S., Scheirer, D.S., Langenheim, V.E., Kohler, M.D., 2012. A new perspective on the geometry of the San Andreas Fault in Southern California and its relationship to lithospheric structure. Bull. Seismol. Soc. Am. 102, 236–251.
Geist, E.L., Andrews, D.J., 2000. Slip rates on San Francisco Bay area faults from anelastic deformation of the continental lithosphere. J. Geophys. Res. 105 (B11), 25543–25552.
Griscom, A., Jachens, R.C., 1990. Crustal and lithospheric structure from gravity and magnetic studies, in the San Andreas Fault System, California. In: Wallace, R.E. (Ed.)U.S. Geological Survey Professional Paper 1515, pp. 239–259.
Harris, R.A., Segall, P., 1987. Detection of a locked zone at depth on the Parkfield, California, segment of the San Andreas Fault. J. Geophys. Res. 92 (B8), 7945–7962.
Hole, J.A., Ryberg, T., Fuis, G.S., Bleibinhaus, F., Sharma, A.K., 2006. Structure of the San Andreas fault zone at SAFOD from a seismic refraction survey. Geophys. Res. Lett. 33, L07312 doi:10.1029/2005GL025194.
Hough, S.E., Ben-Zion, Y., Leary, P., 1994. Fault zone waves observed at the southern Joshua Tree earthquake rupture zone. Bull. Seismol. Soc. Am. 84, 761–767.
Kim, W., Baag, C.-E., 2002. Rapid and accurate two-point ray tracing based on a quadratic equation of takeoff angle in layer media with constant or linearly varying velocity functions. Bull. Seismol. Soc. Am. 92, 2251–2263.
Kim, A., Dreger, D., 2008. Rupture process of the 2004 Parkfield earthquake from near-fault seismic waveform and geodetic records. J. Geophys. Res. 113, B07308 doi: 10.1029/2007JB005115.
Kim, W., Hahm, I.-K., Ahn, S.J., Lim, D.H., 2006. Determining the hypocentral parameters for local earthquakes in 1-D using genetic algorithms. Geophys. J. Int. 166, 590–600.
Kim, W., Hong, T.-K., Kang, T.-S., 2014. Hypocentral parameter inversion for regions with poorly known velocity structures. Tectonophysics 627, 182–192.
Kissling, E., Ellsworth, W.L., Eberhart-Phillips, D., Kradolfer, U., 1994. Initial reference models in local earthquake tomography. J. Geophys. Res. 99, 19635–19646.
Klein, F.W., 1978. Hypocenter location program HYPOINVERSE, U.S. Geological Survey. Open-File Report 78-694, Menlo Park, California (113 pp.).
Klein, F.W., 2002. User's guide to HYPOINVERSE-2000, a fortran program to solve for earthquake locations and magnitudes. U.S. Geological Survey, Open-File Report 02-171, Menlo Park, California (123 pp.).
Korneev, V.A., Nadeau, R.M., McEvilly, T.V., 2003. Seismological studies at Parkfield IX: fault-zone imaging using guided wave attenuation. Bull. Seismol. Soc. Am. 93, 1415–1426.
Lahr, J.C., 1980. HYPOELLIPSE/MULTICS: a computer program for determining local earthquake hypocentral parameters. Magnitude, and First Motion Pattern, US Geological Survey Open-File Report. US Geological Survey, Denver, Colorado, pp. 59–80.
Le Pichon, X., Kreemer, C., Chamot-Rooke, N., 2005. Asymmetry in elastic properties and the evolution of large continental strike-slip faults. J. Geophys. Res. 110, B03405 doi:10.1029/2004JB003343.
Lee, W.H.K., 1990. Replace the HYPO71 format? Bull. Seismol. Soc. Am. 80, 1046–1047.
Lee, W.H.K., Lahr, J.C., 1975. HYPO71 (revised): a computer program for determining local earthquake hypocenter, magnitude, and first motion pattern of local earthquakes. US Geological Survey Open-File Report, 75-311, Melon Park, California (113 pp.).
Lees, J.M., Malin, P., 1990. Tomographic images of P wave velocity variation at Parkfield, California. J. Geophys. Res. 95, 21793–21803.
Lewis, M.A., Ben-Zion, Y., McGuire, J.J., 2007. Imaging the deep structure of the San Andreas Fault south of Hollister with joint analysis of faultzone head and direct P arrivals. Geophys. J. Int. 169, 1028–1042.
Lin, G., Thurber, C.H., Zang, H., Hauksson, E., Shearer, P.M., Wauldhauser, F., Brocher, T.M., Hardebeck, J., 2010. A California statewide three-dimensional seismic velocity model from both absolute and differential times. Bull. Seismol. Soc. Am. 100, 225–240.
Liu, P., Custódio, S., Archuleta, R.J., 2006. Kinematic inversion of the 2004 M 6.0 Parkfield earthquake including an approximation to site effects. Bull. Seismol. Soc. Am. 96, S143–S158.
Louie, J.N., Clayton, R.W., LeBras, R.J., 1988. Three-dimensional imaging of steeply dipping structure near the San Andreas fault, Parkfield, California. Geophysics 53 (2), 176–185.
Lutter, W.J., Fuis, G.S., Ryberg, T., Okaya, D.A., Clayton, R.W., Davis, P.M., Prodehl, C., Murphy, J.M., Langenheim, V.E., Benthien, M.L., Godfrey, N.J., Christensen, N.I., Thygesen, K., Thurber, C.H., Simila, G., Keller, G.R., 2004. Upper crustal structure from the Santa Monica mountains to the Sierra Nevada, southern California: tomographic results from the Los Angeles regional seismic experiment, Phase II (LARSE II). Bull. Seismol. Soc. Am. 94, 619–632.
McPhee, D.K., Jachens, R.C., WentWorth, C.M., 2004. Crustal structure across the San Andreas fault at SAFOD site from potential field and geologic studies. Geophys. Res. Lett. 31 doi:10.1029/2003GL019363.
Michelini, A., McEvilly, T.V., 1991. Seismological studies at Parkfield, part I: simultaneous inversion for velocity structure and hypocenters using cubic B-splines parameterization. Bull. Seismol. Soc. Am. 81, 524–552.
Nadeau, R.M., McEvilly, T.V., 2004. Periodic pulsing of characteristic microearthquakes on the San Andreas Fault. Science 303, 220–222.
NCEDC, 2014. Northern California Earthquake Data Center, UC Berkeley. Dataset doi: 10.7932/NCEDC.
Parsons, T., Hart, P.E., 1999. Dipping San Andreas and Hayward faults revealed beneath San Francisco Bay. Calif. Geol. 27, 839–842.
Schweitzer, J., 1997. HYPOSAT—a new routine to locate seismic events. NORSAR Scientific Report 1.97(98). NORSAR, Norway, pp. 94–102.
Shapiro, N.M., Campillo, M., Stehly, L., Ritzwoller, M.H., 2005. High-resolution surface-wave tomography from ambient seismic noise. Science 307, 1615–1618.
Sieh, K.E., 1978. Slip along the San Andreas Fault associated with the great 1857 earthquake. Bull. Seismol. Soc. Am. 68, 1421–1447.
Simpson, R.W., Barall, M., Langbein, J., Murray, J.R., Rymer, M.J., 2006. San Andreas fault geometry in the Parkfield, California, region. Bull. Seismol. Soc. Am. 6, S28–S37.
Thatcher, W., Grant, M., Lisowski, M., 1997. Resolution of fault slip along the 470-km-long rupture of the great 1906 San Francisco earthquake and its implications. J. Geophys. Res. Solid Earth 102 (B3), 5353–5368.
Thurber, C., Roecker, S., Roberts, K., Gold, M., Powell, L., Rittger, K., 2003. Earthquake locations and three-dimensional fault zone structure along the creeping section of the San Andreas Fault near Parkfield, CA: preparing for SEAFOD. Geophys. Res. Lett. 30 doi:10.1029/2002GL016004.
Thurber, C., Roecker, S., Zhang, H., Baher, S., Ellsworths, W., 2004. Fine-scale structure of the San Andreas fault and location of the SEAFOD target earthquakes. Geophys. Res. Lett. 31, L12S01 doi:10.1029/2003GL019398.
Thurber, C., Zhang, H., Waldhauser, F., Hardebeck, J., Michael, A., Eberhart-Philips, D., 2006. Three-dimensional compressional wavespeed model, earthquake relocations, and focal mechanisms for the Parkfield, California, region. Bull. Seismol. Soc. Am. 96, S38–S49.
Titus, S.J., DeMets, M., Tikoff, B., 2006. Thirty-five-year creep rates for the creeping segment of the San Andreas fault and the effects of the 2004 Parkfield earthquake: constraints from alignment arrays, continuous GPS, and creepmeters. Bull. Seismol. Soc. Am. 96, S250–S268.
Trifunac, M.D., Udwadia, F.E., 1974. Parkfield, California, earthquake of June 27, 1966: a three-dimensional moving dislocation. Bull. Seismol. Soc. Am. 64 (3), 511–533.
Unsworth, M., Malin, P.E., Egbert, G.D., Booker, J.R., 1997. Internal structure of the San Andreas fault at Parkfield. Calif. Geol. 25, 359–362.
Waldhauser, F., Ellsworth, W., 2000. A double-difference earthquake location algorithm: method and application to the northern Hayward fault, California. Bull. Seismol. Soc. Am. 90, 1353–1368.
Waldhauser, F., Ellsworth, W., Schaff, D.P., Cole, A., 2004. Streaks, multiplets, and holes: high-resolution spatio-temporal behavior of Parkfield seismicity. Geophys. Res. Lett. 31, L18608 doi:10.1029/2004GL020649.
Wdowinski, S., Smith-Konter, B., Bock, Y., Sanwell, D., 2007. Diffuse interseismic deformation across the Pacific–North America plate boundary. Geology 35, 311–314.
Zhao, P., Peng, Z., 2008. Velocity contrast along the Calaveras fault from analysis of fault zone head waves generated by repeating earthquakes. Geophys. Res. Lett. 35, L01303 doi:10.1029/2007GL031810.
Zhao, P., Peng, Z., Shi, Z., Lewis, M.A., Ben-Zion, Y., 2010. Variation of the velocity contrast and rupture properties of M 6 earthquake along the Parkfield section of the San Andreas fault. Geophys. J. Int. 180 (2), 765–780.
Zoback, M., Hickman, S., Ellsworth, W., 2010. Scientific drilling into the San Andreas fault zone, Eos, Transactions. Am. Geophys. Union 91 (22), 197–199.